ELSEVIER

Journal of Nuclear Materials 276 (2000) 258–268

journal of nuclear materials

www.elsevier.nl/locate/jnucmat

In situ transmission electron microscopy study of ion-irradiated copper: comparison of the temperature dependence of cascade collapse in fcc- and bcc-metals

T.L. Daulton*, M.A. Kirk, L.E. Rehn

Materials Science Division, Argonne National Laboratory, Argonne IL, 60439, USA

Abstract

The kinetics which drive cascade formation and subsequent collapse into point-defect clusters are investigated by analyzing the microstructure produced in situ by low fluence 100 keV Kr ion irradiations of fcc-Cu over a wide temperature range (18–873 K). The yield of collapsed point-defect clusters is demonstrated unequivocally to be temperature dependent, remaining approximately constant up to lattice temperatures of 573 K and then abruptly decreasing with increasing temperature. This drop in yield is not caused by defect loss during or following ion irradiation. In addition, this temperature dependence can be explained by a thermal spike effect. These in situ yield measurements are compared to previous ex situ yield measurements in fcc-Ni and bcc-Mo.

1. Introduction

The modification of a material's microstructure from ion-beam processing or exposure to high fluxes of energetic particles such as those present in space environments or nuclear reactors can dramatically change the physical properties of the material. Since reactor components are typically exposed to irradiation at elevated temperature, the effects of temperature on irradiation damage mechanisms are of particular interest.

Collision cascades represent the primary mechanism of lattice displacement during high-energy ion and neutron irradiation, and consequently play an important role in the modification of material properties. A displacement collision cascade is a sequence of collisions initiated by a primary knock-on collision which results in a highly disordered region encompassing upwards of several hundred displaced atoms [1,2]. In these events, lattice atoms are ejected from the cascade core and are injected into the immediate surrounding lattice as interstitials. In turn, the core becomes depleted in mass through the associated formation of vacancies. At sufficiently high point-defect concentrations, cascade cores are unstable and point defects recombine or agglomerate into more stable clusters such as various types of dislocation loops and stacking fault tetrahedra (SFT).

The basic mechanisms driving the formation of cascade regions and their evolution into collapsed point-defect clusters are not well understood. This is largely due to the inherent difficulties involved in studying nanometer scaled dynamical processes that evolve on times scales of picoseconds. Rudimentary descriptions of the various atomistic processes which occur during a displacement cascade have been proposed [3–5], although they are insufficient in providing a complete understanding of cascade phenomena. It is the dynamically coupled interaction of these atomistic processes, under non-equilibrium conditions, which ultimately governs cascade development.

Although it is not possible to study directly the basic mechanisms driving the formation of cascade regions and their collapse into point-defect clusters, examination of their product microstructures can reveal information pertaining to these mechanisms. Cascade mechanisms are governed by kinetics and are potentially strongly affected by lattice temperature. Consequently, as the

* Corresponding author. Present address: Marine Geosciences Division, Naval Research Laboratory, Stennis Space Center, MS 39529, USA.

E-mail address: tld@howdy.wustl.edu (T.L. Daulton).

0022-3115/00/$ - see front matter
PII: S0022-3115(99)00185-3

temperature is varied, changes in product microstructures should reflect the manner in which cascade processes depend upon temperature. These changes can include the spatial distribution of point defects within cascade cores and their probabilities of collapse into various types of dislocation loops and SFT. In addition, changes in the distribution of the types of defects produced as well as changes in their respective size distributions can occur. For brevity, the term defect is used here, and from this point forth, to refer collectively to all types of collapsed point-defect clusters.

In this work, the kinetics governing cascade formation and subsequent collapse into defects are studied by analyzing the microstructure produced in situ by 100 keV Kr ion irradiations of fcc-Cu over a wide temperature range (18–873 K) using a transmission electron microscope (TEM). Different complementary TEM techniques are applied to measure the defect yield, defined as the total number of defects formed per incident ion. Defect yield is an important quantity to determine because it is closely related to the probability of cascade collapse, the latter defined as the total number of defects per cascade (including distinct subcascades).

The majority of the previous measurements of defect yield has been made at low temperatures where defects are stable, while only a few studies of yield at elevated temperature have been performed, none of which were in situ, for a review see [6]. The present study is unique in that it is the first study that measures yield at elevated temperatures in situ, a necessity for accurate determinations of the yield. Furthermore, it encompasses the widest temperature range examined, providing a comprehensive picture of cascade collapse which cannot be obtained by comparing individual studies from separate researchers because of the disparities in their experimental conditions. In this work, we establish that the yield of TEM visible defects in Cu is constant below 573 K, above which it rapidly decreases with increasing temperature. We also demonstrate that the probability of cascade collapse must follow a similar temperature dependence. These observations can be explained by a thermal spike effect.

2. Experimental

2.1. Sample preparation

Samples for use in a TEM were prepared from a rolled polycrystalline copper sheet of 99.99% nominal purity and a single crystal copper rod of 99.999% nominal purity. From the polycrystalline sheet and sliced single crystal, 3 mm disks were punched and annealed at 1093 K (0.8 T_{melt}). Electron transparent regions in the annealed disks were prepared by using a South Bay Model 550 single-jet electro-polisher. The typical thickness of the regions examined by TEM were between 500 and 1000 Å. More complete details of the sample preparation are given in [7].

2.2. In situ ion irradiation and characterization

The microscopy was performed in the HVEM-Tandem Facility at Argonne National Laboratory using a Hitachi H-9000NAR TEM interfaced with a 2 MV tandem ion accelerator and a 0.65 MV ion implanter. Further details describing the H-9000NAR TEM/accelerator arrangement are given by [7,8]. The ion implanter was used in these experiments to irradiate Cu specimens with 100 keV Kr ions to a specimen fluence in the range $(9.4 \leqslant \Phi \leqslant 20.4)\times 10^{10}$ ions cm^{-2}. The error estimated for the specimen fluence is between $6\% \leqslant \Delta\Phi/\Phi \leqslant 12\%$, depending upon the particular experimental conditions described in Tables 1 and 2. For fluences of $(9.4 \leqslant \Phi \leqslant 20.4)\times 10^{10}$ ions cm^{-2}, areal densities of non-overlapping cascades are estimated between $(8.7 \leqslant \rho_{\text{isol}} \leqslant 17.4)\times 10^{10}$ cascades cm^{-2} (assuming cascade diameters <100 Å). This corresponds to a cascade overlap of <7% and <15% for the lowest and highest fluences, respectively.

All ion irradiations were conducted in situ within the TEM column. Although the optimum TEM imaging condition is achieved when defects are $\leqslant 100$ Å from the ion-entry surface, the influence of the near surface on the formation and stability of defects is an important concern when the results of thin foil TEM studies are applied to bulk materials. To reduce the influence of the near surface on the cascades, ion-irradiation conditions were chosen to distribute the cascade regions the greatest distance from the ion-entry surface while still maintaining useful image quality. This was achieved by using 100 keV Kr ion irradiations at near normal incidence to the foil while avoiding low index zone axes to circumvent ion-channeling mechanisms which are reported to affect defect yields [9].

Defects resulting from the collapse of cascades were imaged under centered 2-beam dark-field (DF) conditions. With this technique, distinctive high-contrast defect images often termed 'black–white' (BW) contrast images are produced by localized changes in the diffracting conditions caused by lattice strain fields generated by the defects. The image contrast produced is strongly dependent on TEM factors such as the choice of the Bragg diffracted beam, $\boldsymbol{g}$, which is used to form the 2-beam DF image. Of all the possible imaging reflections, $\boldsymbol{g} = (2\,0\,0)$ can produce strong visible B–W contrast for the maximum number of possible defects in Cu: all Frank partial (sessile) dislocation loops ($\boldsymbol{b} = a/3\langle 1\,1\,1\rangle$), all partially dissociated Frank partial (sessile) dislocation loops, four of the six perfect (glissile) dislocation loop Burger's vector variants ($\boldsymbol{b} = a/2\langle 1\,1\,0\rangle$), and all (sessile) SFT.

Table 1
100 keV Kr ion irradiations of fcc-Cu[a]

Ion-irradiation conditions				Extra polation of isothermal data			
Temp. (K)	Fluence Φ ($\times 10^{10}$ Kr/cm^2)	Irradiation time (s) (± 0.05)	Ion-incidence angle θ ($\pm 10^\circ$)	Area analyzed ($\times 10^{-10}$ cm^2)	Surface inclination at imaging φ ($\pm 10^\circ$)	Post-irradiation yield	Post-irradiation yield (Average)
						(Normalized to fluence Φ)	
18	9.6 ± 0.6	6.1	0°	78 ($+10-6$)	27°	1.06 ± 0.13	
294	9.6 ± 0.6	6.5	0°	73 ($+8-5$)	25°	0.98 ± 0.11	1.06 ± 0.10
295	9.6 ± 0.6	11.8	0°	83 ($+12-7$)	31°	0.99 ± 0.13	
295	9.6 ± 0.6	11.0	0°	90 ($+18-11$)	39°	1.05 ± 0.17	
296	9.6 ± 0.6	10.0	1°	82 ($+13-8$)	32°	1.20 ± 0.16	
296	9.6 ± 0.6	12.4	0°	75 ($+9-6$)	26°	1.16 ± 0.13	
573	9.6 ± 0.6	6.3	0°	79 ($+10-6$)	27°	1.03 ± 0.12	
623	9.6 ± 0.6	19.7	0°	76 ($+9-6$)	24°	0.68 ± 0.07	
648	9.6 ± 0.6	4.5	0°	80 ($+11-7$)	30°	0.54 ± 0.07	
673	9.6 ± 0.6	14.2	0°	81 ($+11-7$)	30°	0.50 ± 0.06	
723	9.5 ± 0.6	14.9	8°	87 ($+15-10$)	36°	0.20 ± 0.03	0.21 ± 0.02
723	15.6 ± 0.7	3.7	0°	83 ($+13-8$)	32°	0.23 ± 0.03	
773	14.4 ± 0.7	18.0	0°	115 ($+10-7$)	17°	0.041 ± 0.003	0.041 ± 0.001
773	20.4 ± 0.7	13.7	0°	79 ($+11-7$)	30°	0.040 ± 0.005	
873	14.2 ± 0.8	16.8	10°	129 ($+20-12$)	32°	0.013 ± 0.001	

[a] Illustrated in Fig. 1.

Table 2
100 keV Kr ion irradiations of fcc-Cu

Ion-irradiation conditions				VCR analysis			
Temp. (K)	Fluence Φ ($\times 10^{10}$ Kr/cm^2)	Irradiation time (s) (± 0.05)	Ion-incidence angle θ ($\pm 10^\circ$)	Area analyzed ($\times 10^{-10}$ cm^2)	Surface inclination at imaging φ ($\pm 10^\circ$)	Post-irradiation yield	Integrated yield
						(Normalized to fluence Φ)	
296	9.4 ± 0.7	11.8	12°	7.8 ($+1.1-0.7$)	29°	1.11 ± 0.12	1.12 ± 0.13
573	9.6 ± 0.6	14.4	5°	17 ($+2-1$)	26°	0.88 ± 0.09	0.94 ± 0.10
623	9.5 ± 0.7	7.6	8°	19 ($+3-2$)	36°	0.69 ± 0.09	0.77 ± 0.10
723	9.5 ± 0.7	15.0	10°	52 ($+9-6$)	35°	0.22 ± 0.03	0.39 ± 0.05
773	10.8 ± 0.6	26.0	3°	138 ($+18-12$)	27°	0.032 ± 0.004	0.075 ± 0.009
873	14.1 ± 0.8	17.9	12°	203 ($+31-21$)	32°	0.0056 ± 0.0006	0.018 ± 0.002

Since the majority of possible defect types can be visible under the $\boldsymbol{g}=(2\,0\,0)$ reflection, all 2-beam DF imaging was performed using this reflection at an orientation along the (2 0 0) Kikuchi band typically 20° from the [0 1 1] zone axis. However, perfect loops satisfying the $\boldsymbol{g}\cdot\boldsymbol{b}=0$ condition, defects distributed within boundary layers producing very weak or no visible contrast [10], and defects smaller than the 2-beam DF imaging resolution will not be adequately imaged. Since not all of the defects are visible under the $\boldsymbol{g}=(2\,0\,0)$ reflection, yields determined using solely this imaging condition cannot represent true absolute yields. Nonetheless, from these TEM measured yields important conclusions are reached about the temperature dependence of the absolute yield.

2.3. Determination of defect yield

Representative defect microstructures which are present in Cu shortly after elevated temperature ion irradiations are shown in Fig. 1. Although a marked decrease in defect density is apparent as the ion irradiation is performed on specimens held at progressively higher temperatures, the accurate quantification of the defect

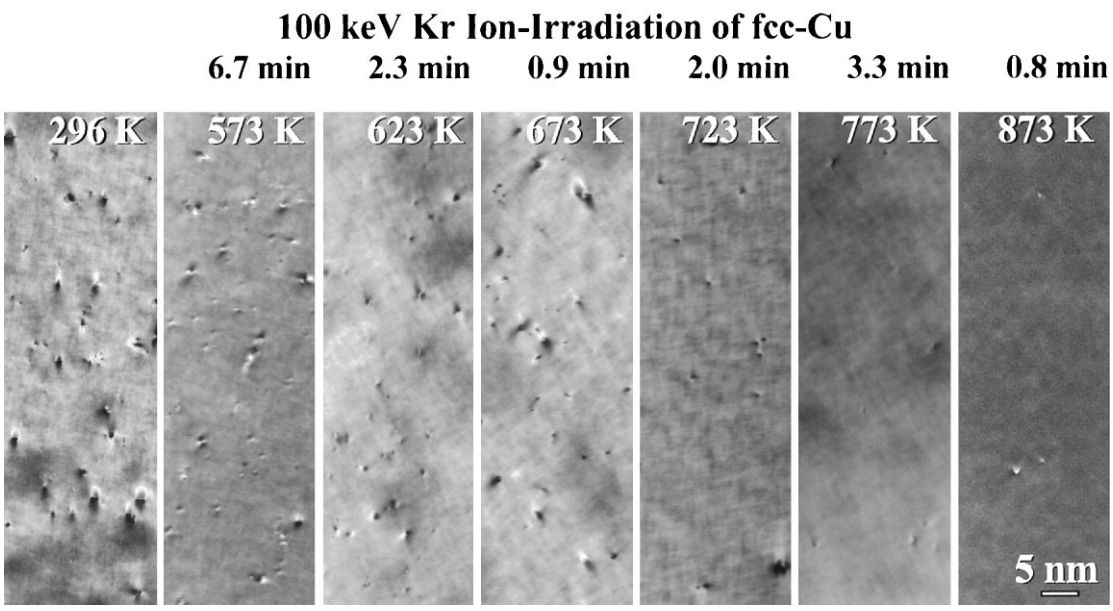

Fig. 1. Dark-field micrographs in negative contrast [using the $\boldsymbol{g} = (2\,0\,0)$ reflection] displaying the representative defect microstructure present several minutes (anywhere from 0.8 to 6.7 min) after the completion of at temperature 100 keV Kr ion irradiation of Cu. Ion fluences are given in Table 1.

yield at elevated temperature is intrinsically difficult to obtain. This is a consequence of the rapid microstructural evolution that occurs under isothermal anneal at elevated temperature which severely limits the extent to which ion induced changes in the microstructure can be characterized by in situ TEM imaging techniques. Microstructures can be well characterized at temperatures where the kinetics are slow. However, it is difficult to achieve sufficiently rapid thermal quenching of the specimen, following ion irradiation, to a temperature which impedes the kinetics before significant microstructural evolution has occurred. Therefore, a significant number of defects are lost during the isothermal anneal following the ion irradiation. Furthermore, defects are lost during ion irradiation and it has been reported that the lifetimes of defects during ion irradiation are considerably shorter than in the absence of irradiation [11].

Previous investigations of defect yield at elevated temperature have been performed ex situ, leaving many details ambiguous. For an accurate determination of defect yield at elevated temperature, isothermal defect losses incurred both during and following ion irradiation need to be determined. This can only be accomplished through TEM microstructural characterization concurrent with, and immediately following, in situ ion irradiations. In this study, both the post-irradiation yield, defined as the number of TEM visible defects per incident ion present immediately after completion of the ion irradiation, and the integrated yield, defined as the total number of TEM visible defects per incident ion formed over the duration of the ion irradiation, were measured. From these, important conclusions regarding the absolute yield were obtained.

2.3.1. Post-irradiation defect yield

At sufficiently high temperatures, defects become unstable and are quickly lost from the foil through various mechanisms. Consequently, at these temperatures, any TEM characterization recorded on micrographs would not be of the product microstructure originally present immediately following the ion irradiation. Therefore, it is necessary to establish the rates at which defects vanish under isothermal anneal before TEM observations can be used to measure the defect yield. Based upon these rates, the defect density (per ion fluence) present immediately following ion irradiation, the post-irradiation yield, can be determined through extrapolation. This is the methodology which was adopted.

Specimens were irradiated with 100 keV Kr ions and immediately following the ($\leqslant 20$ s) ion irradiation, TEM micrographs were recorded from the same area of the specimen at predetermined time intervals during the subsequent isothermal anneal. From these micrographs, the areal defect density (normalized to the incident ion fluence) was measured. A full description of these measurements is given in [7]. The results of the series of elevated temperature irradiations and subsequent isothermal anneals are shown in Fig. 2.

The post-irradiation defect yield at elevated temperature is defined as the areal defect density per ion fluence present immediately after completion of the ion irradiation. The post-irradiation yield can be estimated by extrapolating the defect density, $\rho(t)$, back to $t=0$, eliminating the influence of isothermal anneal losses. However, this extrapolation is naturally dependent upon the expression used to model the loss rate. There are many types of defects which are formed by ion irradiation, and their isothermal loss rates depend upon factors such as their type, size, orientation, and distance from the near surface. The various loss mechanisms include the annihilation of perfect loops upon reaching the surface by glide and the evaporation of Frank loops through point-defect emission. Frank loops can also convert to perfect loops which are then subsequently lost to the surface. Moreover, Frank loops can partially dissociate along intersecting $\langle 1\,1\,1\rangle$ planes and can eventually form SFT, which can also be lost through emission of point defects. Despite the complexity, the general behavior during annealing of the defect ensemble can be approximated by

$$\rho(t) = \sum_{i=1}^{n} \alpha_i \exp(-\beta_i t), \tag{1}$$

where α and β are fitting parameters. Although, this is a simplified model for the loss rate of the total defect population, at most three exponential terms are sufficient to produce fits that agree well with the data.

Post-irradiation yields are determined from extrapolations of the fitted loss models, $\rho(t\to 0)$, for ion irradiations performed at temperatures >350 K, while for lower temperatures, the kinetics are slow enough to allow direct measurement from micrographs recorded shortly after ion irradiation. These values are listed in Table 1 and plotted in Fig. 3. The reported errors reflect only the combined uncertainties in the fluence and area determination. Not included in the error estimations of the yield is an assessment of the accuracy of the extrapolation, $\rho(t\to 0)$, of the simple loss rate model. This is sensitive to the predictability of the loss rate model, to how quickly the first images were recorded following the ion irradiation, and to scatter in the data, particularly early in the anneal ($t<10$ min). There is no straightforward approach to evaluate these factors. However, at temperatures where the experiment was repeated (Fig. 3), consistent post-irradiation yields were obtained, demonstrating the reproducibility of the extrapolation method. Furthermore, in a separate set of experiments

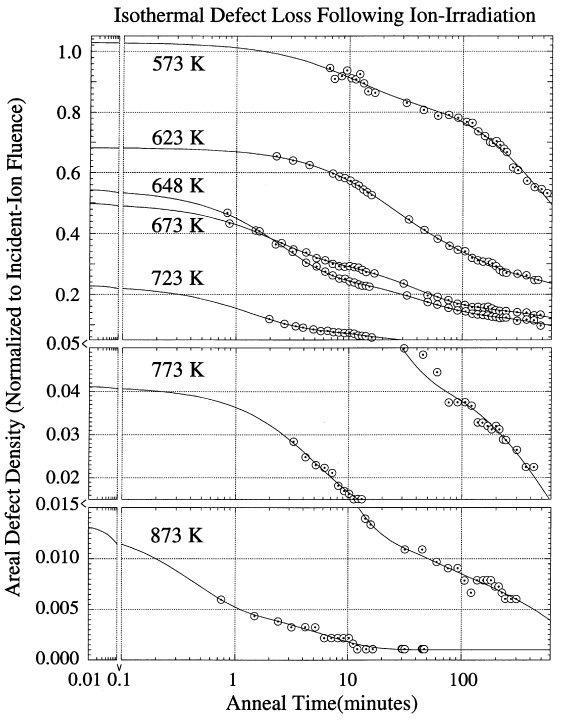

Fig. 2. The areal defect densities present during the isothermal anneal following 100 keV Kr ion irradiations of Cu at temperature, 100 keV. Defect densities are normalized to the incident-ion fluence. The curves represent least squares fits of Eq. (1) to the data. The abscissa is plotted in logarithmic scale to more clearly illustrate the behavior near $t=0$ on the ordinate. At temperatures where the experiment was repeated, one representative data set is plotted.

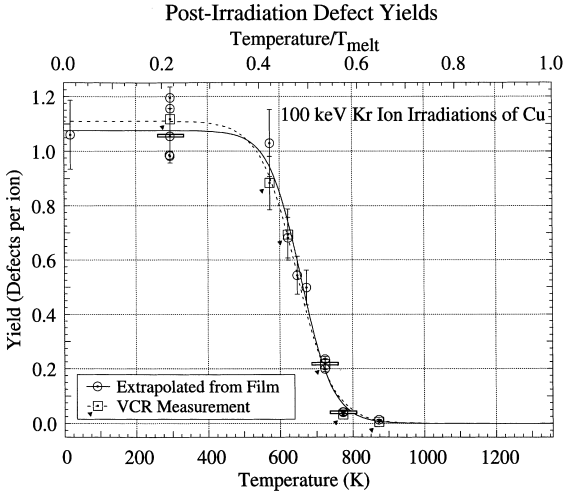

Fig. 3. The post-irradiation defect yield for 100 keV Kr ion-irradiated Cu determined from TEM micrographs (circles) and VCR frames recorded at the completion of the ion irradiation (squares). For multiple measurements at the same temperature, the horizontal bar represents the weighted mean. The curves (*solid* – TEM film and *dashed* – VCR) represent fits to a step function and are used to display the trends in the data.

which is discussed fully in Section 2.3.2, post-irradiation yields were directly measured from VCR recorded images (approximately ±0.1 s following the completion of the ion irradiation). The agreement between the post-irradiation yields estimated using two very different methods, extrapolation of isothermal anneal data and direct measurement of VCR recorded images (Fig. 3), instills confidence in the experimental methodologies and the yield determination.

These measurements demonstrate that the post-irradiation yield exhibits a clear dependence on lattice temperature (Fig. 3), remaining relatively constant from 18 to 573 K, then abruptly decreasing above 573 K. This drop in yield cannot be attributed to annealing losses following ion irradiation. It has been reported that during ion irradiation the lifetimes of defects are considerably shorter, and consequently the loss rate greater, than in the absence of irradiation [11]. The immediate question arises as to whether a temperature dependence for the isothermal loss rate during ion irradiation can account for the change in post-irradiation yield, essentially the mechanism which has been previously attributed to the apparent decline in yield observed earlier in Cu [12]. To adequately resolve this point, it is necessary to observe directly the production and loss of defects during ion irradiation at elevated temperature.

2.3.2. Integrated defect yield during ion irradiation

The formation of defect microstructure during ion irradiation is a dynamic process. Once a defect is formed, its position in the foil as well as its structure (Burger's vector, habit plane, or size) can be altered [13] or even destroyed upon further ion irradiation. The total number of TEM visible defects per incident ion which form during ion irradiation, regardless of whether they survive to the completion of the ion irradiation, is defined as the integrated defect yield.

Integrated yields can only be obtained through analysis of concurrent observations of defect formation during ion irradiation. In this work, this was accomplished through the use of video recordings of 2-beam DF images in the TEM. The temporal resolution of VCR recordings is on the order of one frame every 1/30 s, and consequently, any defects which are formed and lost within a shorter time interval will not be imaged. Although VCR format tape offers substantially increased time resolution over a time sequence of micrographs, its spatial resolution is far inferior to that of conventional film. Small and closely spaced defects arising from subcascades are more difficult to resolve.

From the analysis of the VCR frames recorded during ion irradiations, both the post-irradiation, Y_{Pir}, and the integrated, Y_{Int}, defect yields were determined (Fig. 4 and Table 2). Full details of the measurements are given in [7]. The integrated yields exhibit a similar temperature dependence as that of the post-irradiation yields and

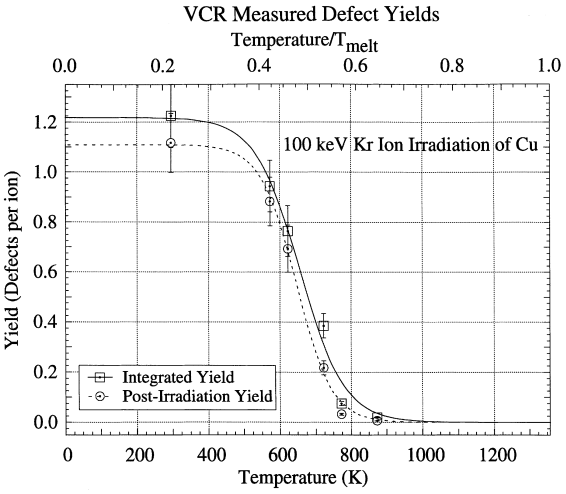

Fig. 4. Integrated (squares) and post-irradiation (circles) defect yields measured by analysis of VCR data for 100 keV Kr ion irradiations of Cu. The curves (*solid* – Y_{Int} and *dashed* – Y_{Pir}) represent fits to a step function and are used to display the trends in the data.

clearly demonstrate that the loss of defects during ion irradiation is insufficient by a large margin to account for the observed decrease in post-irradiation yield with increasing temperature.

2.3.3. Absolute defect yield

The entire defect population will not be visible under any one 2-beam DF imaging condition. Defects will not be adequately imaged if they are distributed within boundary layers producing very weak or no visible contrast, satisfy the $\boldsymbol{g}\cdot\boldsymbol{b}=0$ criterion for low image contrast, or are smaller than the resolution limit for 2-beam DF (<15 Å for this work). Consequently, the yields measured by TEM do not represent absolute yields.

The relationship between the integrated yield and the absolute yield, $Y(T)$, can be written

$$Y_{\mathrm{Int}}(T) = Y(T)[1-\varepsilon_{\mathrm{bl}}(\varphi)][1-\varepsilon_{(\boldsymbol{g}\cdot\boldsymbol{b})}(\boldsymbol{g},T)][1-\varepsilon_{\mathrm{rl}}(T)], \tag{2}$$

where $\varepsilon_{\mathrm{bl}}(\varphi)$ represents the fraction of defects which produce weak to no visible contrast because they are in boundary layers. The term $\varepsilon_{(\boldsymbol{g}\cdot\boldsymbol{b})}(\boldsymbol{g},T)$ represents the fraction of defects produced that is invisible under the operating $\boldsymbol{g}$ 2-beam reflection, and $\varepsilon_{\mathrm{rl}}(T)$ represents the fraction of defects produced with sizes below the resolution limit for 2-beam DF. The latter two terms, $\varepsilon_{(\boldsymbol{g}\cdot\boldsymbol{b})}(\boldsymbol{g},T)$ and $\varepsilon_{\mathrm{rl}}(T)$, are written as functions of temperature since the distributions of defect types and sizes produced by ion irradiations are likely temperature dependent. Rather than accurately measuring

these ε-terms, each of which would require extensive experimental work, it will be shown that they cannot account for the observed decrease in integrated yield, demonstrating that the absolute yield must carry a true temperature dependence.

For any operating $\boldsymbol{g}$ reflection, a considerable fraction of the defects can be distributed within boundary layers producing either weak or no visible B–W contrast. Boundary layers result from the oscillatory dependence of the B–W image contrast on the defect's distance from the near surface [10]. The depth distribution of defects should remain largely unchanged for each temperature examined. However, in our experiments the surface inclination with respect to the 2-beam imaging direction varied between experimental runs (see Table 1). Increasing the surface inclination results in a longer electron path through the foil and consequently moves the boundary layers closer to the foil surface, potentially altering the proportion of visible defects. However, modified TRIM simulations [14,15] indicate that the fraction of uncounted defects lying within the boundary layers should be approximately uniform, $\varepsilon_{\mathrm{bl}}(\varphi) \approx 0.20 \pm 0.02$, for the conditions of our experiments.

Accurate measurements of the fraction of defect types produced at elevated temperature which is invisible under the $\boldsymbol{g} = (2\,0\,0)$ reflection, $\varepsilon_{(\boldsymbol{g}\cdot\boldsymbol{b})}(\boldsymbol{g}, T)$, cannot be readily performed. However, a redistribution of defect types will have a very limited effect on the proportion of invisible defects since the majority of the known possible defect types can produce visible contrast under the operating $\boldsymbol{g} = (2\,0\,0)$ reflection. Therefore, $\varepsilon_{(\boldsymbol{g}\cdot\boldsymbol{b})}(\boldsymbol{g}, T)$ should be roughly constant (≈0.1) for each of the TEM measurements.

An inherent limitation of all TEM yield measurements is that they cannot take into account the fraction of defects, $\varepsilon_{\mathrm{rl}}(T)$, whose size is below the resolution limit for TEM strain-field and stacking-fault contrast. This fraction is naturally dependent on the defect size distribution. It is likely that defect size distributions vary systematically with formation temperature, changing the proportion of defects which are too small to be resolved. A change in the fraction of unresolved defects cannot be directly observed. However, size distributions of visible defects indicated that the defect populations produced at progressively higher temperatures have their median and mode (or peak) in the distribution shifted towards larger defect sizes. Full details of these measurements are given in [7]. Therefore, it is reasonable to infer that the decrease in observed yield with increasing temperature is not a result of an increase in the fraction of defects too small to be resolved.

In summary, a fraction of the defect population produced by ion irradiation is not visible under the TEM imaging conditions of this experiment, and consequently, the defect yields reported here do not represent absolute yields. Nonetheless, we demonstrated that the temperature dependence exhibited by these TEM measured yields must result from a similar temperature dependence of the absolute yield.

2.4. Subcascades and the probability of cascade collapse

In the presence of subcascade formation, the absolute yield, $Y(T)$, is different from the probability of cascade collapse, $\Pi(T)$. This is because the two quantities differ in their normalization term, $Y(T)$ with respect to the total number of ions and $\Pi(T)$ with respect to the total number of cascades (including distinct subcascades). They are related by

$$\Pi(T) = \chi^{-1}(T) Y(T), \tag{3}$$

where $\chi(T)$ is the efficiency of subcascade formation defined as the average number of individual, discrete cascades (or subcascades) formed per incident ion. Eq. (3) assumes that all the defects were formed by the collapse of the vacancy-rich cascade core and neglects possible formation of TEM visible interstitial loops in the cascade periphery. The question of whether or not interstitial loops are formed is still under debate [16,17].

Neither the temperature dependence of subcascade formation nor its mechanisms are well established, because quantitative measurements of $\chi(T)$ as a function of temperature are experimentally difficult to perform, and none have been published. However, it is possible to estimate the maximum possible drop in subcascade formation with increasing temperature.

Binary collision simulations have predicted the formation of ≈3 subcascades per 100 keV recoil at 300 K in Cu [18]. Further, it is reasonable to assume that at 100 keV, an incident ion will produce at least one cascade (equivalent to one subcascade) regardless of temperature. Therefore, the efficiency of subcascade formation cannot decrease by more than a factor of 3 in response to changes in temperature for 100 keV Kr ion irradiations of Cu. In comparison, the decrease in yield in Cu, over the range 18–873 K, is over 2 orders of magnitude. Although a decrease in subcascade formation would reduce the absolute yield, it clearly would fall well short in accounting for all the decline in the yield. Consequently, the maximum possible rate of increase in $\chi^{-1}(T)$ could not offset the measured rate of decrease in $Y(T)$ in Eq. (3). Therefore, the decrease in absolute yield with increasing lattice temperature must correspond to a decrease in the probability of cascade collapse.

3. Comparison to previous experiments

Defect yields have previously been measured at elevated temperature in fcc-Cu [12,19], bcc-Mo [20], and fcc-Ni [21]. However, these measurements were

performed ex situ where defect losses arising from isothermal anneal during and following ion irradiation could only be estimated. For the 30 keV self-ion irradiations of Cu [12,19], a decrease in defect density with increasing irradiation temperature was reported, similar to our observations. However, the relative drop in yield measured between 573 and 673 K in [12] was over a factor of 3.5 greater than that measured here. The yield was defined differently in [19], i.e., as defect clusters per ion, where all defects produced by the same ion represent one defect cluster. Nonetheless, in terms of our yield definition, the relative drop measured in [19] is more than a factor of 4 greater than that measured here. It is possible that the increased proximity of the 30 keV Cu ion cascades to the near surface could have influenced the temperature dependence of the yield, but the apparent increased drop is more likely attributed to anneal losses following ion irradiation. In fact, it was argued that the apparent variation in yield with temperature could be entirely accounted for by defect loss through thermal emission of point defects during the 60 s ion irradiations, arguing against a true temperature dependence for defect yield in Cu [12]. The drop in yield observed in 80 keV W ion-irradiated Ni was also attributed to loss through isothermal anneal [21]. Unfortunately, the unknown isothermal anneal losses incurred as these samples cooled ($\approx$50 K min^{-1} for [12]) following the ex situ ion irradiation preclude any meaningful comparative interpretation of the yields measured at different temperatures for any particular material.

The elevated temperature yield measurements for 60 keV self-ion irradiations of bcc-Mo [20] did offer better insights into cascade processes. A decrease in yield was reported at temperatures below which significant defect loss from isothermal anneal was observed. This provided the first indication that the cascade collapse process was temperature dependent, at least for bcc-Mo.

4. Comparison to the thermal spike model

Molecular dynamics simulations, which model many-body collisions for a set of particles interacting through a specified interatomic potential, have revealed that cascades exhibit distinct stages of development [22]. The first phase is ballistic in nature and is often termed the collisional spike because the energy of the primary knock-on atom is rapidly distributed by multiple collisions among many atoms within the cascade volume. These lattice displacements result in the ejection of atoms from the cascade core into the periphery as interstitials while creating associated vacancies within the core. At the beginning of the collisional spike phase, the total energy of the cascade region is predominately in the form of the kinetic energy possessed by the atoms undergoing multiple collisions. The point at which the injected energy of the incident ion becomes equally distributed between the kinetic and potential components of the crystal energy can be perceived as the final stage of the cascade evolution. At this point, the heat-flow mechanisms which dissipate the potential energy from the cascade region become increasingly important, and the cascade enters what is referred to as the thermal spike phase.

In the thermal spike phase, large energy densities remain within the cascade core which can extend into the surrounding lattice. It was suggested that an incident ion could deposit energy densities sufficiently high enough to cause local melting of the cascade core [23]. This conjecture was later supported by molecular dynamics simulations in Cu where radial distribution functions calculated for the cascade core during the thermal spike were similar to those calculated for a liquid [24]. This led to the idea that solidification of the liquid-like (or quasi-molten) cascade core could lead to vacancies being concentrated at the center [25]. Further, it was proposed that the rate of thermal quenching largely controls the spatial evolution of core vacancies and, ultimately, cascade collapse [26]. It was argued that solidification would proceed inwards from the interface between the bulk thermal reservoir and the quasi-molten zone [26]. Under sufficiently rapid solidification rates, vacancies would be quenched into the lattice and distributed throughout the solidified core. On the other hand, a high degree of crystalline order would result for slow solidification rates since the vacancies would be swept ahead of the solidification front and concentrated at the cascade center. Slow solidification would favor cascade collapse because a concentrated region of vacancies would have a higher driving force for collapse. Assuming equilibrium heat transport, the solidification rate should depend on the temperature differential between the quasi-molten zone and the bulk. Therefore, this mechanism alone would predict that defect yield should increase with increasing temperature across the entire temperature range.

Support for the model of [26] is found at low temperature in Ni [27] and Cu_3Au [28], where the defect yield at 30 K is less than at 300 K. However, in Cu we observed that the defect yield at 18 K is nearly the same as that at 300 K. Our observation does disagree with the earlier, although limited, low temperature measurements of 50 keV Kr ion-irradiated Cu [13], where the yield at 30 K was a reported to be a factor of 2 less than that at 300 K. Our higher yield at low temperature cannot be attributed to misidentification of hydrocarbon surface contamination as defects since surface mobility is low near liquid-helium temperatures and this impedes the buildup of contamination. Our higher yield cannot be explained by a fluence error, since this possibility was ruled out by repeating the experiment. However, the

measurement of artificially lower yields can be easily explained if the defects were under counted in the earlier work of [13]. In this regard, we note that they used a TEM and a liquid-helium stage with lower defect resolution than in our work.

Mechanisms which concentrate vacancies at the center of the cascade core are usually evoked to drive core collapse. Our observations suggest that for Cu either these mechanisms are not strongly affected by temperature below 300 K or alternatively are not required for cascade collapse. If cascade collapse is only triggered when the vacancy concentration is locally very high, our observed yields at 18 K would then suggest that either the vacancy sweeping during solidification is not impeded by the near liquid-helium temperatures of the surrounding lattice or that other mechanisms for concentrating vacancies are active.

The concept of a quasi-molten zone can explain the important observation of a rather abrupt onset of the rapid decrease in defect yield with increasing lattice temperature. Following the collisional spike, a quasi-molten zone can develop within the cascade region. The volume of this quasi-molten zone would depend on the specific heat of the lattice, the heat of transformation, and the rate of heat transport to the surrounding lattice. Therefore, the maximum volume that the quasi-molten zone achieves should increase as the lattice temperature increases, and this idea is supported by recent molecular dynamics simulations of the cascades in α-Fe [29].

At low lattice temperatures, the thermal quench rate should be high and restrict the quasi-molten zone to the center of the cascade region. Interstitials can then escape the periphery of the vacancy rich cascade core by thermal diffusion. As the lattice temperature is increased, the maximum volume of the quasi-molten zone will increase. At the temperature where the quasi-molten zone extends into the interstitial-rich periphery, a significant amount of interstitials will be annihilated in the quasi-melt before they can escape the periphery. In turn, the density of the quasi-melt will increase and fewer vacancies will form upon solidification. Since all molecular dynamic simulations indicate that the interstitial-rich region of the cascade periphery radially extends through only several adjacent lattice sites, a very rapid decrease in defect yield with further increases in temperature should result. In other words, once the quasi-molten zone reaches the thin interstitial-rich shell, many more interstitials are engulfed with small increases in the quasi-melt volume. However, the inherent distribution of cascade sizes and shapes would tend to widen the temperature range in which a rapid decline in yield is observed. Consistent with this model, the temperature profile which is observed for the yield resembles an elongated step function (Figs. 3 and 4). The center of this step function we define as the yield threshold temperature.

5. Comparison to other metals

The thermal-spike model naturally predicts that with higher melting temperatures, the yield threshold temperature should be greater. This is because higher temperatures are needed to extend the quasi-molten volume into the interstitial-rich region. Both the melting temperature (1726 K Ni and 1357 K Cu) and the yield threshold temperature (≈776 K for Ni [21], and 653 ± 6 K for Cu, see Figs. 3 and 4) are greater in Ni than in Cu. Further, the ratios between Ni and Cu in melting and yield threshold temperatures roughly scale with one another; 1.27 and ≈1.19, respectively. However, the agreement is probably even closer. The Ni yield measurements were performed ex situ and isothermal anneal losses could not be taken into account. Such losses would shift the measured yield threshold temperature to smaller values. For example, the threshold temperature suggested by the ex situ measurements of Cu in [12] is ≈619 K, 0.95 of that measured in this work. If the threshold temperature suggested for Ni is scaled by 1/0.95 to approximately account for annealing losses, the ratio between the threshold temperatures for Ni and Cu becomes 1.25. This is close to the ratio of their melting temperatures. Therefore, the rapid decline in yield observed in Ni in [21] is also consistent with the thermal-spike model.

The temperature dependence of the yield in bcc-Mo [20] differs significantly from that of both fcc-Ni [21] and fcc-Cu (Fig. 5). Although the melting temperature of Mo (2890 K) is over twice that of Cu, the onset of the decline in defect yield was observed to occur slightly above 300 K [20]. Furthermore, the drop in yield in Mo

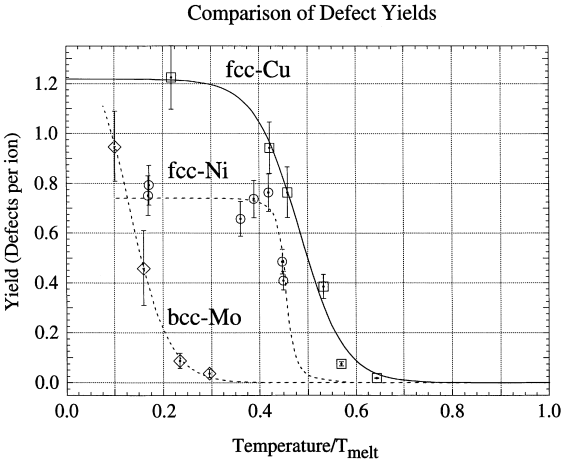

Fig. 5. Comparison of the elevated temperature yields measured in fcc-Cu (Y_{Int} – squares), fcc-Ni [21] (circles) and bcc-Mo [20] (diamonds). The latter two were measured ex situ and their dashed curves display the trends in the data. The abscissa is plotted in terms of the melting temperature of the metal.

is more gradual as compared to the sharp drop observed in Ni and Cu. For example, the width of the temperature interval over which an order of magnitude drop in defect yield occurs is roughly 550 K for Mo (see [20]) compared to 170 K for Cu (see Figs. 3 and 4). This suggests that recombination of interstitials resulting from the quasi-melt volume extending into the interstitial-rich periphery is not responsible for the observed drop in yield in Mo. Another mechanism must greatly reduce the yield at temperatures below which the thermal-spike volume can expand sufficiently and affect cascade collapse.

6. Summary

The yield of TEM visible defects produced from in situ 100 keV Kr ion irradiation of Cu was measured over a wide lattice temperature range (18–873 K). Importantly, these are the first measurements which have taken account of isothermal anneal losses during and following ion irradiation. Defect yields are demonstrated unequivocally to be temperature dependent, remaining approximately constant up to lattice temperatures of 573 K and then abruptly decreasing with increasing temperature. This is a true drop in yield and not an artifact caused by defect loss during or following ion irradiation. Furthermore, it was shown that this variation with temperature must result from a temperature dependence for the probability of cascade collapse into defect clusters.

Our measurements of elevated temperature yield provide support for the thermal-spike model. At elevated temperature, the abrupt and rapid decline in defect yield and probability of cascade collapse observed in Cu can be attributed to the annihilation of interstitials resulting when the quasi-molten volume extends into the thin interstitial-rich shell surrounding the cascade. The previous yield measurements in Ni are also consistent with this model. However, the previous yield measurements in bcc-Mo suggest that a lower temperature mechanism is responsible for significantly decreasing the yield before the quasi-melt volume can affect cascade collapse at higher temperatures.

Acknowledgements

The electron microscopy and ion irradiations were performed in the HVEM-Tandem facility at Argonne National Laboratory. From the HVEM-Tandem facility, the authors thank E.A. Ryan and S. Ockers for valuable assistance and L.L. Funk for the operation of the ion-accelerator used in these experiments. The authors thank B.J. Kestel for valuable assistance with sample preparation. The authors also thank M.L. Jenkins for valuable comments and kindly providing single-crystal copper. The authors also thank H. Fukushima for valuable discussions. This research was supported by US DOE under BES contract W-31-109-ENG-38.

References

[1] J.A. Brinkman, J. Appl. Phys. 25 (1954) 961.
[2] J.A. Brinkman, Am. J. Phys. 24 (1956) 246.
[3] R.H. Silsbee, J. Appl. Phys. 28 (1957) 1246.
[4] A. Seeger, Proceedings of the Second UN International Conference on Peaceful Uses of Atomic Energy, vol. 6, Geneva, UN, New York, 1958, p. 250.
[5] A. Seeger, Radiation Damage in Solids, vol. 1, IAEA, Vienna, 1962, p. 101.
[6] M.L. Jenkins, M.A. Kirk, W.J. Phythian, J. Nucl. Mater. 205 (1993) 16.
[7] T.L. Daulton, M.A. Kirk, L.E. Rehn, Philos. Mag. A (1999), in press.
[8] C.W. Allen, L.L. Funk, E.A. Ryan, Mater. Res. Soc. Symp. Proc. 396 (1996) 641.
[9] M.T. Robinson, O.S. Oen, Phys. Rev 132 (1963) 2385.
[10] M. Rühle, Radiation Damage in Reactor Materials Proc. Symp., vol. 1, Vienna: International Atomic Energy Agency, 1969, p. 113.
[11] S. Ishino, N. Sekimura, K. Hirooka, T. Muroga, J. Nucl. Mater. 141–143 (1986) 776.
[12] C.A. English, B.L. Eyre, J. Summers, Philos. Mag. 34 (1976) 603.
[13] J.S. Vetrano, I.M. Robertson, M.A. Kirk, Scripta Met. Mater. 24 (1990) 157.
[14] M.W. Bench, I.M. Robertson, M.A. Kirk, Nucl. Instrum. and Meth. B 59–60 (1991) 372.
[15] M.C. Frischherz, M.A. Kirk, J.P. Zhang, H.W. Weber, Philos. Mag. A 67 (1993) 1347.
[16] H. Fukushima, M.L. Jenkins, M.A. Kirk, Philos. Mag. A 75 (1997) 1567.
[17] H. Fukushima, M.L. Jenkins, M.A. Kirk, Philos. Mag. A 75 (1997) 1583.
[18] H.L. Heinisch, B.N. Singh, Philos. Mag. A 67 (1993) 407.
[19] M. Wilkens, Fundamental Aspects of Radiation Damage in Metals, Proceedings of an International Conference held at Gatlinburb, Tennessee, 6–10 October 1975, CONF-751006-P1, p. 98.
[20] C.A. English, B.L. Eyre, A.F. Bartlett, H.N.G. Wadley, Philos. Mag. 35 (1977) 533.
[21] T.M. Robinson, M.L. Jenkins, Philos. Mag. A 43 (1981) 999.
[22] M.W. Guinan, H.H. Kinney, J. Nucl. Mater. 103–104 (1981) 1319.
[23] F. Seitz, J.S. Koehler, in: F. Seitz, D. Turnbull, (Eds.), Solid State Physics, vol. 2, Academic Press, New York, 1956, p. 305.
[24] T. Diaz de la Rubia, R.S. Averback, P. Benedek, W.E. King, Phys. Rev. Lett. 59 (1987) 1930.
[25] D.N. Seidman, R.S. Averback, R. Benedek, Phys. Stat. Sol. 144 (1987) 85.
[26] T. Diaz de la Rubia, R.S. Averback, H. Hsieh, R. Benedek, J. Mater. Res. 4 (1989) 579.

[27] M.A. Kirk, I.M. Robertson, M.L. Jenkins, C.A. English, T.J. Black, J.S. Vetrano, J. Nucl. Mater. 149 (1987) 21.
[28] T.J. Black, M.L. Jenkins, C.A. English, M.A. Kirk, Proc. Roy. Soc. London A 409 (1987) 177.
[29] F. Gao, D.J. Bacon, P.E.J. Flewitt, T.A. Lewis, J. Nucl. Mater. 249 (1997) 77.